Dalton Transactions

ROYAL SOCIETY OF CHEMISTRY

PAPER

View Article Online
View Journal | View Issue

Cite this: *Dalton Trans.*, 2025, **54**, 14367

Role of heteroatom substitution on the stability and reactivity of mononuclear Cu(II)–alkylperoxo complexes

Limashree Sahoo, [a] Yi Zhang,[b,c] Amrit Das, [a] Sam P. de Visser *[a,b,c] and Chivukula V. Sastri *[a]

Motivated by copper's essential role in biology and its wide range of applications in catalytic and synthetic chemistry, this work aims to understand the effect of heteroatom substitution on the overall stability and reactivity of biomimetic Cu(II)–alkylperoxo complexes. In particular, we designed a series of tetracoordinated ligand frameworks based on iso-BPMEN = (*N*,*N*-bis(2-pyridylmethyl)-*N*′,*N*′-dimethylethane-1,2-diamine) with varying the primary coordination sphere using different donor atoms (N, O, or S) bound to Cu(II). The copper(II) complexes bearing iso-BPMEN and their modified heteroatom-substituted ligands were synthesized and structurally characterized. These novel complexes are manifested as biomimetic models of enzymatic copper(II) complexes that typically bind the metal through some neutral and anionic amino acid side chains. The *in situ* generated Cu(II)–alkylperoxo intermediates were spectroscopically characterized and evaluated for their stability and reactivity. The stability and reactivity of copper(II)–alkylperoxo intermediates exhibited diverse behaviors depending on the ligand. Interestingly, the reactivity for the S- and O-coordinated Cu(II)–alkylperoxo intermediates exhibited significantly higher (200–300 fold) electrophilic heteroatom oxidation efficiency compared to the N-bound Cu(II)–alkylperoxo species. Computational studies further support a mechanism involving O–O bond homolysis, followed by efficient oxygen atom transfer. These findings suggest that heteroatom substitution plays a crucial role in fine-tuning the oxidation chemistry of copper(II) complexes, enhancing their potential as biomimetic models for copper-based oxidation reactions.

Received 29th July 2025,
Accepted 29th August 2025

DOI: 10.1039/d5dt01804h

rsc.li/dalton

Introduction

Copper ions, abundant in the Earth's crust, are fundamental to various biological processes such as oxygen transport, catalysis, and electron transfer. As a consequence, copper-containing proteins function as a defence mechanism against oxidative damage but also assist with growth and biosynthesis reactions.[1] Several mononuclear copper enzymes, such as peptidylglycine α-hydroxylating monooxygenase (PHM), dopamine β-monooxygenase (DβM), lytic polysaccharide monooxygenases (LPMOs), and galactose oxidase (GO), utilize O_2-derived reactive species to carry out oxidative transformations on diverse biological substrates (Scheme 1).[2] These enzymes share a primary coordination sphere around the Cu center composed of a mix of neutral and anionic donors, including nitrogen (from histidine), sulfur (from methionine), and oxygen (from tyrosine or carbonyl groups).[2] In PHM and DβM, two non-coupled binuclear copper enzymes are proposed to form a reactive Cu-superoxo species utilizing dioxygen and enabling the hydroxylation reaction.[2c,e] In LPMOs, which feature a mononuclear copper centre coordinated by a histidine brace, the resting Cu(I) reacts with O_2 (or H_2O_2) to form a Cu-oxyl or Cu-superoxo species, enabling hydrogen atom abstraction from polysaccharide C–H bonds, followed by hydroxylation and glycosidic bond cleavage.[2d,e] By contrast, galactose oxidase operates *via* a Cu(II)-tyrosyl radical cofactor, which abstracts a hydrogen atom from the substrate alcohol to form an aldehyde and reduced cofactor, which is then reoxidized by O_2.[2e] These natural systems underscore the versatility of copper–oxygen chemistry and highlight how the ligand environment, whether composed of histidine, methionine, or tyrosine, can significantly influence the redox properties and reactivity of Cu–O_2 intermediates.[2] Importantly, this biological insight motivates the design of biomimetic copper catalysts that replicate the function of these enzymes. Synthetic copper-coupled oxidations have gained

[a]*Department of Chemistry, Indian Institute of Technology Guwahati, Assam 781039, India. E-mail: sastricv@iitg.ac.in; Fax: +91-361-258-2349*
[b]*Manchester Institute of Biotechnology, The University of Manchester, 131 Princess Street, Manchester M1 7DN, UK. E-mail: sam.devisser@manchester.ac.uk*
[c]*Department of Chemical Engineering, The University of Manchester, Oxford Road, Manchester M13 9PL, UK. E-mail: sam.devisser@manchester.ac.uk*

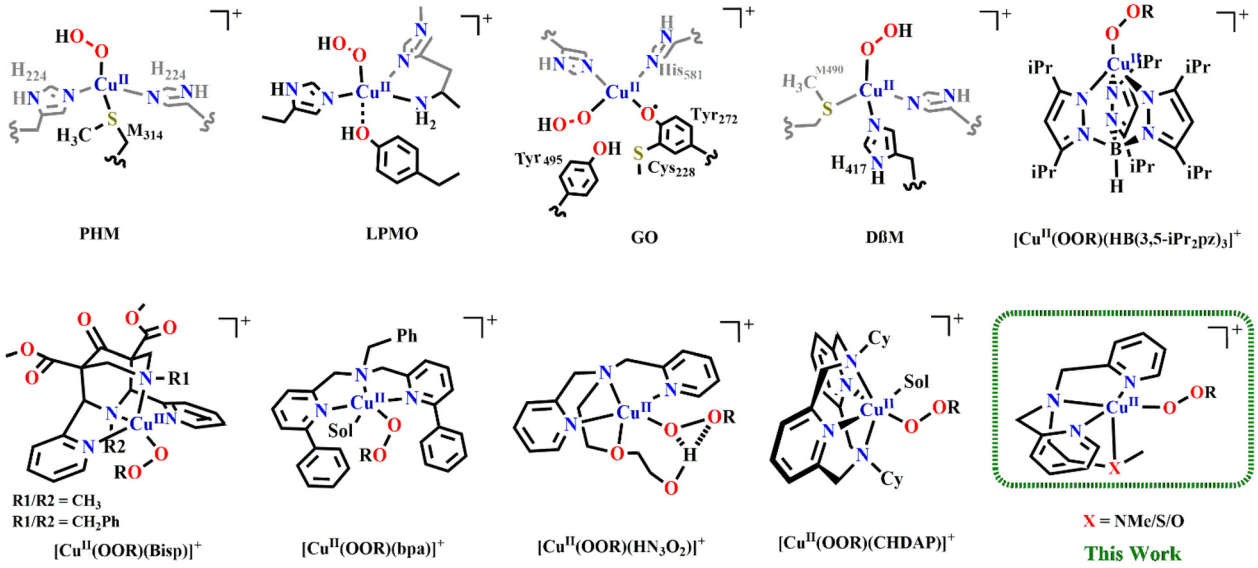

Scheme 1 Proposed Cu(II)–hydroperoxo intermediates in selected copper monooxygenase enzymes and some examples of reported bioinspired Cu(II)–alkylperoxo systems that are discussed in the literature.

significant attention across scientific disciplines, partly due to their biological relevance and ability to carry out diverse functional group transformations.[3] The wide range of biological and synthetic Cu-coupled oxidations showcases how the reactivity of copper centres can be finely tuned by coordinated ligands through steric and electronic effects.[4] Even subtle alterations in the ligand environment can lead to changes in reaction pathways and mechanisms.[5] Therefore, the ligand framework and the first coordination sphere around copper centres are critically important for activity and catalysis.

Among the diverse Cu–O_2 species accessible in both biological and synthetic contexts, copper–alkylperoxo species have emerged as particularly important intermediates. Their biological relevance is highlighted by the fact that copper ions are frequently employed to initiate lipid peroxidation in model systems, such as in studies of low-density lipoprotein oxidation.[6] Significant advancements in the trapping and characterization of copper(II)–alkylperoxo species have been made (Scheme 1) and particularly following Kitajima's pioneering work, which involved the structural characterization of a mononuclear copper(II)–alkylperoxo intermediate with a hydrotris(pyrazolyl)borate ligand.[7] Detailed spectroscopic studies and investigations into the reactivity of Cu(II)–alkylperoxo intermediates have since been conducted by Solomon and co-workers.[8] Tolman and co-workers made advances by characterizing both copper(II)- and copper(III)–alkylperoxo complexes and exploring their reactivity toward substrates with relatively weak C–H or O–H bonds, revealing both electrophilic and nucleophilic behavior.[9] Itoh *et al.* examined the electrophilic reactivity of copper(II)–alkylperoxo complexes that were triggered by O–O bond homolysis forming the reactive Cu(II)–O$^{\bullet}$ species.[10] Additionally, studies have demonstrated that copper(II)–alkylperoxo complexes can conduct nucleophilic reactions.[11] In particular, the studies focused on the effects of hydrogen bonding interactions of the substrate with Cu(II)–alkylperoxo intermediates, and how this influences the reactivity in oxygen atom transfer, C–H activation, and aldehyde deformylation.[12] Researchers have also investigated the effects of ligand rigidity and denticity on the mechanism of O–O bond cleavage using Cu(II)–alkylperoxo intermediates with (N_2/Py_2) tetradentate ligands.[13] Previously, our group synthesized a Cu(II)–alkylperoxo intermediate with bispidine ligand framework and studied the electrophilic aldehyde deformylation, and electrophilic oxygen atom transfer reactivity with a selection of substrates.[14] Most of the Cu(II)–alkylperoxo intermediates are typically recognized for their electrophilic reactivity toward organic substrates, which is facilitated by the homolytic or heterolytic cleavage of the O–O bonds.[10,12,15] In recent years, biomimetic models have been developed that include axial and equatorial heteroatom substitutions to influence reactivity and the mechanisms of reactions.[16]

Such heteroatom substitutions significantly impact nonheme iron complexes by altering their electronic structure, ligand field, redox properties, and capabilities for secondary interactions. By taking inspiration from the natural copper enzymes and the heteroatom substituted model systems, we systematically replaced axial nitrogen atom with sulphur and oxygen in the parent copper(II) *iso*-BPMEN (*N*,*N*-bis(2-pyridylmethyl)-*N*′,*N*′-dimethylethane-1,2-diamine) complex and examined the three corresponding Cu(II)–alkylperoxo intermediates to further understand how the axial heteroatom substitution influences their overall stability and reactivity.

Results and discussion

Our study started with the synthesis of the tetradentate ligand frameworks, namely L^{NMe_2} (*N*,*N*-dimethyl-*N*′,*N*′-bis(pyridin-2-

ylmethyl)ethane-1,2-diamine), L^{SMe} (2-(methylthio)-*N*,*N*-bis (pyridin-2-ylmethyl)ethan-1-amine), and L^{OMe} (2-methoxy-*N*,*N*-bis(pyridin-2-ylmethyl)ethan-1-amine). The ligand L^{NMe_2} was synthesized using a previously reported procedure,[17] while the other two ligands (L^{SMe} and L^{OMe}) were synthesized according to slightly modified protocols (see SI for detailed experimental protocols and synthesis schemes, Schemes S1 and S2).

The corresponding copper(II) complexes were prepared by the dropwise addition of $Cu^{II}(ClO_4)_2{\cdot}2CH_3CN$ to the ligand solution in acetonitrile at room temperature and stirred overnight. Upon ether layering of the reaction mixtures blue powders for each of the three complexes were obtained. The copper(II) complexes, $[Cu^{II}(L^{NMe_2})]^{2+}$ (**1a**), $[Cu^{II}(L^{SMe})]^{2+}$ (**2a**), and $[Cu^{II}(L^{OMe})]^{2+}$ (**3a**), were thoroughly characterized by UV-visible spectroscopy (UV-vis), electrospray ionization mass spectrometry (ESI-MS), cyclic voltammetry (CV), electron paramagnetic resonance spectroscopy (EPR) and single-crystal X-ray crystallography (see Fig. S1–S18 in the SI). The UV-Vis spectra of the three copper(II) complexes at 298 K revealed weak d–d transitions ranging 600–950 nm with distinct molar absorption coefficients (ε), see Table 1 and Fig. S10. Complex **1a** exhibited three weak d–d transition bands at 649 nm (ε = 89 M^{-1} cm^{-1}), 778 nm (ε = 124 M^{-1} cm^{-1}), and 937 nm (ε = 101 M^{-1} cm^{-1}). Similar bands were obtained for complex **2a**, namely at 635 nm (ε = 120 M^{-1} cm^{-1}), and 790 nm (ε = 100 M^{-1} cm^{-1}), Complex **3a**, by contrast, displayed a single d–d band at 623 nm (ε = 98 M^{-1} cm^{-1}), see Table 1. Clearly, the changes in the absorption spectra suggest the structural modifications, in particular, the higher centrosymmetricity in **3a** compared to **1a** and **2a**. The additional shoulders in the visible to NIR region are also indicative of the existence of the latter two in a typical Cu(II) square pyramidal orientation. The slight shift in the d–d transition at around 623 nm clearly indicate the influence of the axial heteroatom substitution that induces major changes to the electronic environment around the Cu(II) centre. The complexes were further characterized using ESI-MS at 298 K. The positive mode ESI-MS for the three complexes gave major signals at *m*/*z* 433.18, 436.01, and 420.18 for **1a**, **2a**, and **3a** respectively (Fig. S11–S13), corresponding to the $[Cu^{II}(L^{NMe_2})(ClO_4)]^+$, $[Cu^{II}(L^{SMe})(ClO_4)]^+$ and $[Cu^{II}(L^{OMe})(ClO_4)]^+$, ionization respectively.

The X-band EPR spectra of the frozen CH_3CN solutions of each complex displayed axial signals with a $g_x = g_y$ value of 2.12 or 2.11, and g_z = 2.55 indicative of a mononuclear Cu(II) centre with a d^9 configuration and $S = \frac{1}{2}$ spin state (Fig. S1). As such, the ligand change has not affected the spin state ordering of the complexes. To further understand the influence of heteroatom coordination to the copper(II) centre, we conducted cyclic voltammetry (CV), and differential pulse voltammetry (DPV) studies of the three Cu(II) complexes. Notably, complex **1a** exhibited an irreversible redox couple with $E_{1/2}$ at −0.140 V (*vs.* Ag/Ag^+). In contrast, substituting L^{NMe_2} with a ligand containing one –S or –O atom produced reversible/quasi-reversible $Cu^{I/II}$ redox couples. Furthermore, replacing NMe with –S or –O resulted in the overall increase of the $Cu^{I/II}$ redox potentials by approximately 0.178 V and 0.136 V for complexes **2a** and **3a**, respectively. Among these, the sulphur-substituted complex **2a** displayed the highest redox potential, with a difference of 0.042 V between **2a** and **3a**, highlighting the distinct electrochemical behaviour influenced by the heteroatom substitution in the first coordination sphere of the metal ion (Table 1 and Fig. S15).

Table 1 Spectroscopic and electrochemical characterization of Cu(II) complexes

Complexes	λ_{max} in nm (ε in M^{-1} cm^{-1})	*g* value	$E_{1/2}$[a] (V)
(**1a**)	649 (89),778 (124),937 (101)	2.12, 2.55	−0.140
(**2a**)	635(120),790 (100)	2.12, 2.55	0.038
(**3a**)	623 (98)	2.11, 2.55	−0.004

[a] Measured *versus* the Ag/Ag^+ couple.

The new complexes **1a**, **2a**, and **3a** were structurally characterized by single-crystal X-ray diffraction (XRD), see Fig. 1, which confirmed the tetra-coordination of ligands L^{NMe_2}, L^{SMe}, and L^{OMe}, where the NMe_2, SMe and OMe groups are orthogonal with respect to the plane through the other four nitrogen atoms, *i.e.* they are located in the axial ligand position (Fig. 1 and Fig. S16–S18). All three complexes have an acetonitrile molecule coordinated in the equatorial plane, while the sixth coordination site is vacant in **1a** and **2a** and occupied with a water molecule in **3a**. Thus, there are structural differences among the three complexes, whereby **1a** and **2a** exist in a C_{4v} point group (distorted square pyramidal) while the complex **3a** remains as O_h (distorted octahedron). Distinct axial bond lengths for Cu1–N1, Cu1–S1, and Cu1–O1 in **1a**, **2a** and **3a** were obtained as 2.258 Å, 2.620 Å, and 2.363 Å, respectively, typical of a Cu(II) d^9 configuration that are susceptible to the Jahn–Teller tetragonal elongation. The Cu1–S1 bond length is in fact, specifically longer also due to the added atomic radius of the sulfur atom. The bond angles ∠N2–Cu1–$NCCH_3$ are 176°, 177°, and 171° for complexes **1a**, **2a**, and **3a**, respectively. Additional bond angles and bond lengths indicate that complexes **1a** and **2a** adopt a distorted square pyramidal geometry with a τ value of 0.37 for **1a** and 0.30 for **2a**, whereas **3a** exhibits a distorted octahedral geometry.[18] Further bond angles and bond lengths are detailed in SI (Tables S1–S5).

With well-characterized Cu(II) precursor complexes on hand, we generated the Cu(II)–alkylperoxo intermediates in acetonitrile at room temperature using cumene hydroperoxide as the external oxidant. The corresponding Cu(II)–alkylperoxo intermediates were generated upon addition of 5 equiv. of cumene hydroperoxide to the solution containing Cu(II) precursor complexes of **2a** and **3a** in the presence of 1.5 equiv. of triethylamine as a base in acetonitrile at room temperature. By contrast, for **1a**, the corresponding alkylperoxo species was only formed when we used 10 equiv. of triethylamine as base and 20 equiv. of cumyl hydroperoxide. In all cases, the addition of cumene hydroperoxide led to an instant change in colour of the solution from blue to light green. The resulting green species were stable with a half-life ($t_{1/2}$) of 24 hours in the case of $[Cu^{II}(L^{NMe_2})(OOCm)]^{2+}$ (**1b**), while the $t_{1/2}$ of the

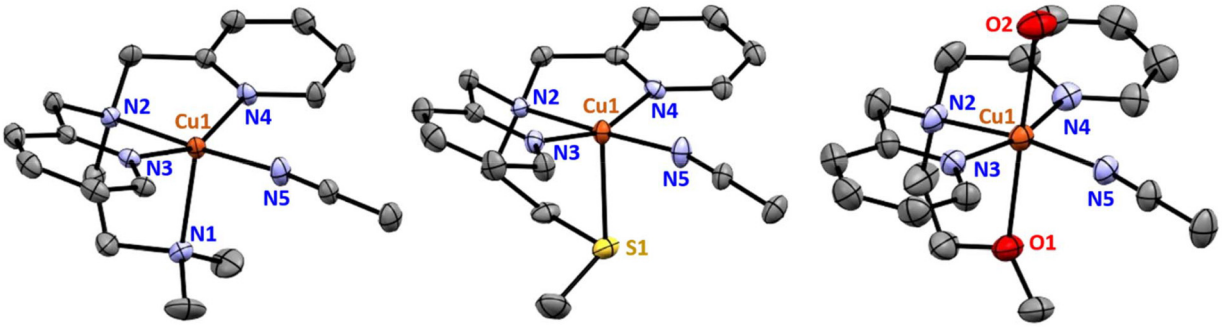

Fig. 1 ORTEP diagrams (with 30% ellipsoid probability) of $[Cu^{II}(L^{NMe_2})]^{2+}$ (**1a**), $[Cu^{II}(L^{SMe})]^{2+}$ (**2a**) and $[Cu^{II}(L^{OMe})]^{2+}$ (**3a**). Colour coding: carbon (grey), copper (orange), nitrogen (blue) oxygen (red), and sulphur (yellow). Hydrogen atoms and counterions have been omitted for clarity.

other two alkylperoxo species $[Cu^{II}(L^{SMe})(OOCm)]^{2+}$ (**2b**) and $[Cu^{II}(L^{OMe})(OOCm)]^{2+}$ (**3b**) were found to be 22 min and 3 hours at 298 K, respectively. The *in situ* generated alkylperoxo species were further characterized by various spectroscopic tools including UV-visible spectroscopy (UV-vis), electron paramagnetic resonance spectroscopy (EPR), electrospray ionization mass spectrometry (ESI-MS), and resonance Raman (*r*R) (see Table 2, Fig. 2 and Fig. S19–S27).

The UV-vis spectra of the copper(II)–alkylperoxo intermediates exhibited distinct ligand-to-metal charge transfer (LMCT) bands. Intermediate **1b** showed an LMCT band at 419 nm (ε = 780 M^{-1} cm^{-1}) along with weaker d–d bands at 642 nm (ε = 169 M^{-1} cm^{-1}) and broad shoulder features extending into the NIR region (700–1000 nm). For **2b**, the LMCT band was observed at 430 nm (ε = 1022 M^{-1} cm^{-1}) with additional weak bands at 632 nm (ε = 231 M^{-1} cm^{-1}) along with similar NIR shoulder bands. In the case of **3b**, an LMCT band appeared at 403 nm (ε = 1175 M^{-1} cm^{-1}) accompanied by a weak band at 573 nm (ε = 157 M^{-1} cm^{-1}), see Fig. 2a, Table 2 and Fig. S19–S21. Substituting nitrogen with sulphur in the ligand framework caused a red shift around 10 nm in the LMCT band, while substitution with oxygen led to a blue shift around 16 nm, indicating the significant electronic influence of the heteroatom on the Cu(II) centre. The observed variations in LMCT band positions and intensities likely arise from differences in ligand field strength and donor ability among the N, S, and O donors. These UV-vis spectral features align with previously reported Cu(II)–alkylperoxo intermediates.[10a,14,19]

The X-band EPR spectra of frozen acetonitrile solutions containing **1b**, **2b** and **3b** were measured at 77 K and show an axial signal with $g_x = g_y = 2.05$ and $g_z = 2.29$ (A_z = 200 G), $g_x = g_y = 2.04$ and $g_z = 2.29$ (A_z = 200 G) and $g_x = g_y = 2.03$ and $g_z = 2.29$ (A_z = 200 G), respectively (see Fig. 3b and Fig. S22). These EPR spectra indicate a structural shift from the precursor Cu(II) complexes, consistent with previously reported findings suggesting a square bipyramidal geometry around the Cu(II) centre in these Cu(II)–alkylperoxo intermediates.[10a,19] ESI-MS analysis of the Cu(II)–alkylperoxo intermediates **1b**, **2b**, and **3b** revealed major peaks at *m*/*z* 484.15, 487.17, and 471.15, corresponding to the species $[Cu(L^{NMe_2})(OOCm)]^+$, $[Cu(L^{SMe})(OOCm)]^+$, and $[Cu(L^{OMe})(OOCm)]^+$, respectively clearly indicating that there is no "S" atom oxidation taking place in L^{SMe} ligand. (Table 2 and Fig. S23–S25). Additionally, we performed Resonance Raman (*r*R) spectroscopy of **1b**, **2b** and **3b** as it is known to have better resolution and favourable selection rules to characterize the vibrational signatures of O–O and Cu–O bonds.[10b,c,11,12,20] The *r*R spectra of complexes **1b**, **2b**, and **3b** were recorded in acetonitrile at 298 K using 473 nm excitation, confirming the formation of Cu(II)–cumylperoxo intermediates. The spectra of all three Cu(II)–alkylperoxo complexes exhibited similar vibrational features (Fig. S26–S28). For **3b**, prominent bands were observed at 877, 833, 659, 594, and 528 cm^{-1} (Fig. 2c and Table 2). Notably, these bands were absent in the blank mixture containing only triethylamine and cumyl hydroperoxide, further validating the assignment to the Cu(II)–OOR intermediates (see Fig. S26–S28). The bands at 877 and 833 cm^{-1} are attributed to mixed O–O, C–O, and C–C vibrations, while the band at 659 cm^{-1} corresponds to the Cu–O stretching mode. Additional bands at 594 and 528 cm^{-1} are assigned to C–C–C and C–C–O deformation modes, consistent with previously reported data for analogous complexes.[10a,11,12,19a]

In the absence of the crystal data structure for Cu(II)–alkylperoxo intermediates, density functional theory (DFT) calcu-

Table 2 Spectroscopic properties, the complex lifetime and its second-order rate constant with PPh_3 as measured for the Cu(II)–alkylperoxo intermediates **1b**, **2b**, and **3b**

Complexes	λ_{max}[a] (nm)	*g* value	*m*/*z*	V_{Cu-O} (cm^{-1})	V_{O-O} (cm^{-1})	$k_{2(PPh_3)}$ (M^{-1} s^{-1})	$t_{1/2}$
(**1b**)	419 (780), 642 (169)	2.29, 2.06	484.15	656	880, 833	0.104	24 h
(**2b**)	430 (1022), 632 (231)	2.29, 2.04	487.17	660	880, 833	22	22 min
(**3b**)	403 (1175), 573 (157)	2.29, 2.03	471.14	659	877, 833	31	3 h

[a] Values in parenthesis are molar absorbance coefficients in M^{-1} cm^{-1}.

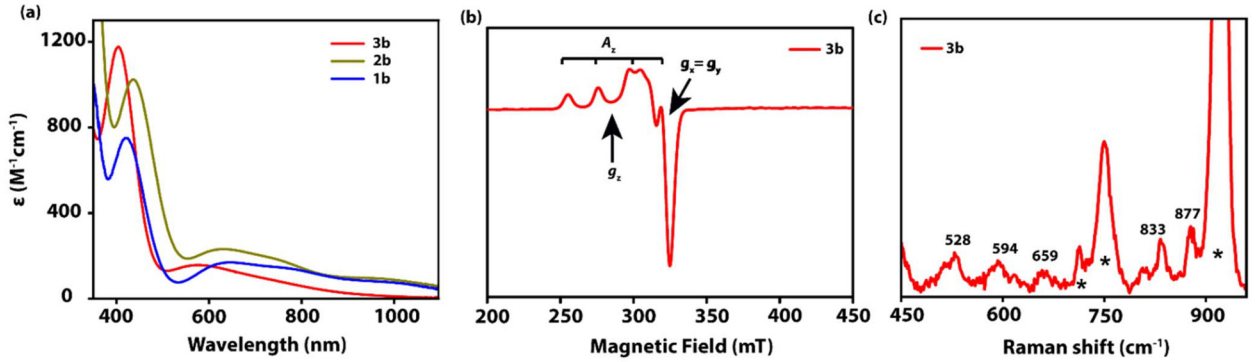

Fig. 2 (a) Overlay of the UV-vis spectra of **1b**, **2b** and **3b** in CH_3CN at 298 K (each of 1 mM). (b) X-band EPR spectra of frozen acetonitrile solution of **3b** at 77 K. (c) Resonance Raman (*r*R) spectra of **3b** (4 mM), which were obtained upon excitation at 473 nm in CH_3CN at 298 K (*denotes residual solvent peak).

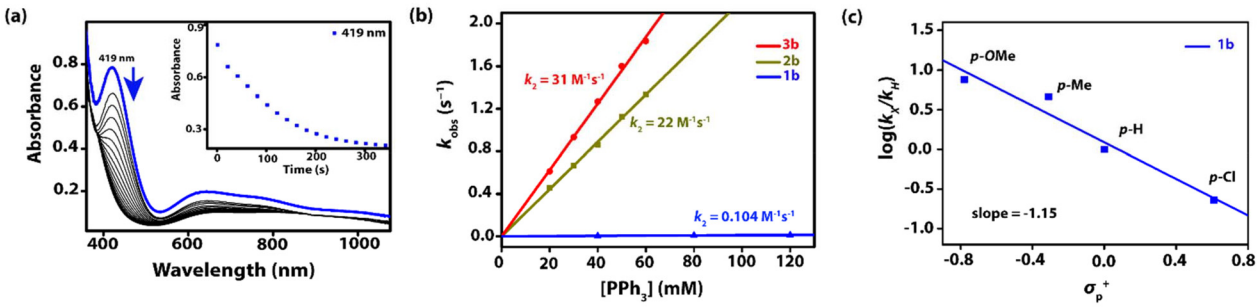

Fig. 3 (a) UV-Vis spectrum for decay of **1b** (1 mM) at 298 K upon addition of PPh_3 (80 mM) in CH_3CN at a scanning interval of 10 s [inset shows the time trace for the peak at 419 nm]. Blue is the starting curve and black are the traces at subsequent time intervals. (b) Second-order rate constants were determined for the reaction of PPh_3 with **1b** (blue line), **2b** (olive line), and **3b** (red line). (c) Plot of $\log(k_X/k_H)$ against the σ_p^+ value of *para*-X substituted PPh_3 for the reaction of **1b**.

lations were performed at the UB3LYP-GD3BJ/BS1 level of theory to obtain insight into the structural parameters of the **1b**, **2b**, and **3b** complexes (see Fig. S29). The bond lengths for DFT optimized **1b**, **2b**, and **3b** intermediates for Cu–N1, Cu–S1, and Cu–O1 were 2.32 Å, 2.689 Å, and 2.39 Å respectively. These bond length trends align with those found in the crystal structure data of the Cu(II) complexes **1a**, **2a**, and **3a**, reported above and in Table S4. The calculated angle along the *z*-axis shows a trend consistent with those observed for the **1a**, **2a**, and **3a** complexes. Thus, examining the bond lengths and angles of the corresponding Cu(II)–alkylperoxo intermediates indicates minimal changes in the geometrical parameters compared to the initial Cu(II) precursor structure. The O–O bond lengths of **1b**, **2b**, and **3b** were found to be 1.44 Å in each case, which is in line with previously reported Cu(II)–alkylperoxo complexes.[7,11]

After the successful characterization of the three intermediates, we then tried to test their oxidative reactivity by taking triphenylphosphine (PPh_3) as the model substrate. Upon the addition of 60 equiv. of triphenylphosphine (PPh_3) in CH_3CN to solutions of **1b**, spectroscopic changes were observed in the UV-vis spectrum and the absorption band at 419 nm decayed as a function of time (Fig. 3a). The pseudo-first-order rate constants (k_{obs}) were determined by pseudo-first-order fitting of the kinetic data for the disappearance at 419 nm for **1b**. The second-order rate constants, k_2, were then determined by varying the concentration of PPh_3 proportionally and for **1b** a value of $k_{2,\mathbf{1b}}$ = 0.104 M^{-1} s^{-1} was obtained. However, upon addition of even 5 equiv. of PPh_3 to either **2b** or **3b** resulted in the immediate decay (in less than 10 s) of the LMCT band, indicating the highly reactive nature of these intermediates. To obtain the second-order rate constants for **2b** and **3b**, we then employed a rapid stopped-flow mixture coupled to a Cary-60 spectrophotometer. The pseudo-first-order rate constants (k_{obs}), were determined by monitoring the disappearance of the LMCT bands at 430 nm for **2b**, and 403 nm for **3b**, respectively. When the PPh_3 concentration was changed, we observed a significantly enhanced reaction rate for heteroatom-substituted Cu(II)–alkylperoxo intermediates as compared to their nitrogen analogue. The second-order rate constants (k_2) were determined to be 24 M^{-1} s^{-1} for **2b**, and 31 M^{-1} s^{-1} for **3b** (Fig. 3b, Fig. S29 and S30). Product analysis of the reaction mixtures revealed triphenylphosphine oxide as the major product (Fig. S31).

To further investigate the influence of electronic effects on the reactivity of **1b**, **2b** and **3b**, a series of *p*-substituted-tri-

phenylphosphine derivatives P(*para*-X-Ph)$_3$ (X = OCH_3, CH_3, H and Cl) were employed. The k_{obs} values for the *para*-substituted triarylphosphines increased linearly with increasing concentration of the substrates, and second-order rate constants were obtained from the plots (Tables S7–S9). When $\log(k_X/k_H)$ *versus* σ_p^+ was plotted, a negative ρ value of −1.15, −1.37 and −0.92 was obtained for **1b**, **2b** and **3b**, respectively in the Hammett plot (Fig. 3c and Fig. S33 and S34), indicating the electrophilic oxygen atom transfer character of the oxidation reaction of triarylphosphines.[12] The variation in ρ values indicates that the electronic properties of the heteroatom substitution significantly affect the electrophilic oxygen atom transfer (OAT) reactivity of the Cu(II)–alkylperoxo complexes. These results clearly demonstrate that heteroatom substitution in Cu(II)–alkylperoxo intermediates with PPh_3 shows a 200–300 times faster reactivity than that of their nitrogen analogues, *i.e.* **1b**. Among the heteroatom-substituted Cu(II)–alkylperoxo intermediates, complex **3b** exhibited a reactivity rate approximately 1.3 times faster than that of **2b**. As we move from nitrogen to sulphur and oxygen in our ligand systems, an increase in reactivity is observed, consistent with findings from our previous studies and literature suggesting that reactivity escalates with the addition of heteroatoms.[16a,e,21] In our recent work, we demonstrated that systematically substituting nitrogen with sulphur and oxygen in iron(II) bispidine complexes resulted in a nearly 15-fold increase in reactivity for chlorite oxidation compared to their nitrogen analogues, while the overall reaction mechanism remained unchanged.[19] Furthermore, we recorded a ninefold acceleration in the rate of sulfoxidation reactions involving sulphur-containing systems relative to nitrogen systems. In our earlier studies on understanding the role of heteroatom substitution, there was a notable shift in the reaction mechanism in two-electron oxidation reactions.[16g] However, no such difference in the reaction mechanism was observed in the case of Cu(II)–alkylperoxo intermediates.

To gain further insight into the nature of the copper(II)–alkylperoxo complexes we calculated two possible dissociation channels, namely heterolytic cleavage of the Cu–O bond to form the complexes **1a**/**2a**/**3a** and ROO^- and the homolytic cleavage of the O–O bond to form the corresponding copper-oxo complexes and $RO^\bullet$ with R = $C(CH_3)_2Ph$, see Fig. 4. We also tested homolytic cleavage of the Cu–O bond and the heterolytic cleavage of the O–O bond and find both mechanisms endergonic by ΔG > 70 kcal mol^{-1}. Consequently, both of these reaction channels were discarded. Nevertheless, for all systems the heterolytic cleavage of the Cu–O bond is still energetically demanding and will require more than ΔG > 50 kcal mol^{-1}. No transition states for these dissociative reactions could be located due to the facile nature of the bond cleavage steps. As such, the copper(II)–alkylperoxo species will be stable and will not self-decay to **1a**, **2a** or **3a** by spontaneous Cu–O bond cleavage and the release of ROO^- anions. These results are consistent with experimental observation that detected no ROO^- or $RO^\bullet$ products in the reaction mixture.

We then explored the O–O cleavage pathways from **1b**, **2b** and **3b** in the doublet spin state and located transition state structures ^{2}**TS1$_{OO}$** for all three systems. Relatively high free energies of activation are found of $\Delta G^\ddagger$ = 34.4, 33.0 and 37.8 kcal mol^{-1}, respectively. These results imply that the O–O cleavage will be slow at room temperature and in an endothermic process leads to a copper-oxo species and $RO^\bullet$ radical. As the O–O cleavage is endergonic, the substrate will need to be located inside the solvent cage of the reactant complex to be able to react with the short-lived copper-oxo species. The overall O–O cleavage barrier is the lowest for **2b**, which is in agreement with the fastest reaction measured with PPh_3.

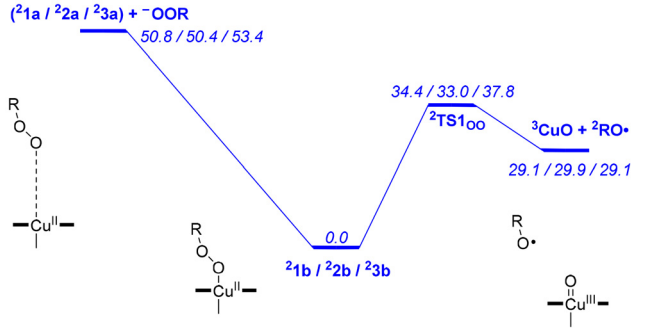

Fig. 4 UB3LYP-GD3BJ/BS1 calculated free energies (in kcal mol^{-1} at 298 K) for Cu–O and O–O cleavage pathways in **1b**, **2b** and **3b**. All structures are the result of a full geometry optimization with a solvent model included.

Conclusions

In this study, three copper(II)–alkylperoxo intermediates, **1b**, **2b**, and **3b** were generated and spectroscopically characterized. Substitution of nitrogen with sulphur and oxygen led to UV-vis spectral shifts, namely a red shift with sulphur and a blue shift with oxygen yet showed no changes in the resonance Raman data, indicating comparable O–O and Cu–O bond energies among all three Cu(II)–alkylperoxo intermediates. The stability and electrophilic oxidation reaction studies showed a varying trend. It was observed that systematic substitution of nitrogen with heteroatom sulphur and oxygen in the axial plane of the copper(II)–alkylperoxo resulted in an overall decrease in the stability of the alkylperoxo intermediates (**1b** > **3b** > **2b**) while to an increase in the atom transfer reactivity (**1b** < **2b** < **3b**). The decrease in the stability and over 200–300 times increase in the reactivity could be attributed to the electronic effects of the heteroatom on the Cu(II) centre. From the computational study, it has been found that the electrophilic oxidation reactions of **1b**, **2b**, and **3b** proceed *via* O–O bond homolysis, followed by efficient oxygen atom transfer to the phosphine substrates.

Experimental

Materials and methods

All reagents were of the highest commercial grade and utilized without additional purification. Solvents were dried according

to the previously published procedure and distilled under argon before use.[27] The ligands L^{NMe_2} were synthesized by slight modification of previously reported procedure;[17] L^{SMe}, and L^{OMe} were newly synthesized. The corresponding copper(II) complexes were prepared using acetonitrile as the solvent. Alkylperoxo copper complexes $[Cu^{II}(L^{NMe_2})(OOCm)]^+$ (**1b**), $[Cu^{II}(L^{SMe})(OOCm)]^+$ (**2b**) and $[Cu^{II}(L^{OMe})(OOCm)]^+$ (**3b**) were generated from their Cu(II) precursors, using 5 equiv. of cumene hydroperoxide (CmOOH) and 1.5 equiv. of triethylamine (TEA) in CH_3CN at 298 K. The detailed experimental procedure is available in the SI.

Instrumentation

UV-visible spectra and kinetic studies were conducted using a Hewlett-Packard 8453 spectrophotometer, which was paired with either a constant temperature circulating water bath or a liquid nitrogen cryostat (Unisoku) controlled by a temperature regulator. Kinetic experiments involving **2b** and **3b** with PPh_3 were carried out using an SFA 20 rapid kinetics accessory (Hi-Tech Scientific pneumatic drive unit) in conjunction with a Cary 60 spectrophotometer. NMR spectra (^1H and $^{13}C\{^1H\}$) were obtained from Bruker Avance III HD 400 MHz and 600 MHz NMR spectrometers, with tetramethylsilane (TMS) as the internal standard. X-band electron paramagnetic resonance (EPR) measurements were performed at 77 K in an acetate buffer solution using a JES-FA200 ESR spectrometer, maintaining experimental parameters as follows: frequency at 9138.66 MHz, power at 0.995 mW, field centre at 490.00 mT, width ±500.00 mT, sweep time of 30.0 s, modulation frequency of 100.00 kHz, width at 2 mT, amplitude for CH1 = 25.0, CH2 = 2.0, and a time constant of 0.03 s, consistent across all samples. High-resolution electrospray ionization mass spectrometry (ESI-MS) spectra were recorded on an Agilent G6546 series UHPLC-LC/Q-TOF-HRMS mass spectrometer at 298 K, utilizing a 140 V nozzle voltage and a gas temperature of 325 °C. Electrochemical measurements, including cyclic voltammetry and differential pulse voltammetry, were performed in dry, degassed acetonitrile using a CH Instruments electrochemical workstation (CHI 1120B). This setup featured a glassy carbon working electrode, a platinum wire auxiliary electrode, and an Ag/AgCl reference electrode, with 0.1 M tetrabutylammonium perchlorate in acetonitrile as the electrolyte. All values were reported against Ag/Ag^+ and calibrated using the Fc^+/Fc couple. Resonance Raman spectra for **1b**, **2b**, and **3b** were recorded at an excitation wavelength of 473 nm (80 mW, Cobolt lasers, HÜBNER Photonics) with a Kymera 328i motorized Czerny-Turner Spectrograph (Andor Technology), equipped with a DU 420A-BEX2-DD camera (iDus 420 CCD, Andor Technology) that was cooled to 193 K. The spectral slit width was set to 120 μm. Single crystal data for $[Cu^{II}(L^{NMe_2})]^{2+}$ (**1a**), $[Cu^{II}(L^{SMe})]^{2+}$ (**2a**), and $[Cu^{II}(L^{OMe})]^{2+}$ (**3a**) were collected at room temperature using a Super Nova CCD System from Agilent Technologies, which featured a fine focus 1.75 kW sealed tube with Mo-Kα radiation. The data reduction was performed using CrysAlis RED, while structure solution and refinement were conducted with the SHELXL97 and Olex2 1.5 software. The crystal structures have been submitted to the CCDC repository. Elemental analysis of ligands and corresponding copper(II) complexes were obtained using VarioMICRO superuser having serial no.: 15181026.

Reactivity studies

All the kinetics were conducted in a 1.0 cm path length UV cuvette, monitoring the UV-Vis spectral changes of a 1.0 mM acetonitrile solution of the complex upon the addition of an excess amount of substrate. The second-order rate constants were calculated by plotting the observed pseudo-first-order rate constants against varying substrate concentrations. The constants were averaged from three determinations, with the standard deviation being less than 10% of the reported values.

Computational methodology

The DFT calculations were performed using Gaussian 09 software.[22] The optimizations were performed using the dispersion corrected unrestricted UB3LYP-GD3BJ density functional method with the LANL2TZ+ basis set with core potential on copper and 6-311+G* basis set on the rest of the atoms abbreviated as BS1.[23,24] Following the optimization analytic frequency calculations were also performed to check the structures to be local minima. All the calculations were performed in the solvent phase with a dielectric constant mimicking acetonitrile using a conductor-type polarized continuum model.[25] The methods were previously tested and validated, demonstrating their ability to reproduce experimentally determined free energies of activation within a few kcal mol^{-1} and to accurately predict the structure.[5f,16g,26]

Author contributions

Conceptualisation: L. S. and C. V. S., data curation: L. S., Y. Z., investigation (experimental work): L. S., and A. D., investigation (computational work): Y. Z., and S. P. de V., methodology: L. S., A. D., Y. Z., formal analysis: L. S., Y. Z., C. V. S., and S. P. de V., funding acquisition: C. V. S., supervision: C. V. S., and S. P. de V., writing – original draft: L. S., writing – Review & Editing: L. S., Y. Z., C. V. S., and S. P. de V.

Conflicts of interest

There are no conflicts to declare.

Data availability

The data underlying this study are available in this article and its SI.

Supplementary information: experimental and computational data, including Cartesian coordinates of optimized structures. See DOI: **https://doi.org/10.1039/d5dt01804h**.

CCDC 2394154–2394156 for **1a**, **2a**, **3a** contain the supplementary crystallographic data for this paper.[28a–c]

Acknowledgements

Research support was provided to C. V. S. by the Department of Science and Technology (SERB), India through the grant code CRG/2023/000456. C. V. S. also acknowledges funding through the Scheme for Transformational and Advanced Research in Sciences MoE/STARS/2023-0374. We would also like to thank Central Instrument Facility, IIT Guwahati for the Instrumental support. SdV thanks the Computational Shared Facilities at the University of Manchester for CPU time and IIT Guwahati for a Visiting Professorship. L. S. and A. D. would like to thank MHRD for the fellowship and the Chemistry department for NMR. We would also like to acknowledge the supercomputing facility provided by IITG through PARAM-ISHAN and PARAM-KAMRUPA. The authors would also like to express their gratitude to Dr. Apparao Draksharapu and Pragya Arora at IIT Kanpur for their assistance with the rR experiment.

References

1 (*a*) K. A. Magnus, H. Ton-that and E. Carpenter, *Chem. Rev.*, 1994, **94**, 727; (*b*) B. G. Malmström and J. Leckneri, *Curr. Opin. Chem. Biol.*, 1998, **2**, 286; (*c*) S. E. Kesler and B. H. Wilkinson, *Geology*, 2008, **36**, 255; (*d*) C. J. Coates and H. Decker, *Cell. Mol. Life Sci.*, 2017, **74**, 293.

2 (*a*) S. T. Prigge, A. S. Kolhekar, B. A. Eipper, R. E. Mains and L. M. Amzel, *Science*, 1997, **278**, 1300; (*b*) J. P. Klinman, *J. Biol. Chem.*, 2006, **281**, 3013; (*c*) K. Yoshizawa, N. Kihara, T. Kamachi and Y. Shiota, *Inorg. Chem.*, 2006, **45**, 3034; (*d*) P. H. Walton and G. J. Davies, *Curr. Opin. Chem. Biol.*, 2016, **31**, 195; (*e*) E. I. Solomon, D. E. Heppner, E. M. Johnston, J. W. Ginsbach, J. Cirera, M. Qayyum, M. T. Kieber-Emmons, C. H. Kjaergaard, R. G. Hadt and L. Tian, *Chem. Rev.*, 2014, **114**, 3659.

3 (*a*) L. M. Mirica, X. Ottenwaelder and T. D. P. Stack, *Chem. Rev.*, 2004, **104**, 1013; (*b*) E. A. Lewis and W. B. Tolman, *Chem. Rev.*, 2004, **104**, 1047; (*c*) L. Q. Hatcher and K. D. Karlin, *Adv. Inorg. Chem.*, 2006, **58**, 131.

4 P. K. Tandon and S. B. Singh, *J. Catal. Catal.*, 2014, **1**, 21.

5 (*a*) T. A. Jackson, J.-U. Rohde, M. S. Seo, C. V. Sastri, R. DeHont, A. Stubna, T. Ohta, T. Kitagawa, E. Münck, W. Nam and L. Que Jr., *J. Am. Chem. Soc.*, 2008, **130**, 12394; (*b*) J.-G. Liu, T. Ohta, S. Yamaguchi, T. Ogura, S. Sakamoto, Y. Maeda and Y. Naruta, *Angew. Chem., Int. Ed.*, 2009, **48**, 9262; (*c*) D. C. Lacy, R. Gupta, K. L. Stone, J. Greaves, J. W. Ziller, M. P. Hendrich and A. S. Borovik, *J. Am. Chem. Soc.*, 2010, **132**, 12188; (*d*) A. Takahashi, D. Yamaki, K. Ikemura, T. Kurahashi, T. Ogura, M. Hada and H. Fujii, *Inorg. Chem.*, 2012, **51**, 7296; (*e*) I. Prat, L. Gómez, M. Canta, X. Ribas and M. Costas, *Chem. – Eur. J.*, 2013, **19**, 1908; (*f*) G. Mukherjee, J. K. Satpathy, U. K. Bagha, M. Q. E. Mubarak, C. V. Sastri and S. P. de Visser, *ACS Catal.*, 2021, **11**(15), 9761.

6 M. J. Burkitt, *Arch. Biochem. Biophys.*, 2001, **394**, 117.

7 N. Kitajima, T. Katayama, K. Fujisawa, Y. Iwata and Y. Moro-oka, *J. Am. Chem. Soc.*, 1993, **115**, 7872.

8 P. Chen, K. Fujisawa and E. I. Solomon, *J. Am. Chem. Soc.*, 2000, **122**, 10177.

9 B. D. Neisen, N. L. Gagnon, D. Dhar, A. D. Spaeth and W. B. Tolman, *J. Am. Chem. Soc.*, 2017, **139**, 10220.

10 (*a*) A. Kunishita, H. Ishimaru, S. Nakashima, T. Ogura and S. Itoh, *J. Am. Chem. Soc.*, 2008, **130**, 4244; (*b*) A. Kunishita, J. Teraoka, J. D. Scanlon, T. Matsumoto, M. Suzuki, C. J. Cramer and S. Itoh, *J. Am. Chem. Soc.*, 2007, **129**, 7248; (*c*) I. Shimizu, Y. Morimoto, G. Velmurugan, T. Gupta, S. Paria, T. Ohta, H. Sugimoto, T. Ogura, P. Comba and S. Itoh, *Chem. – Eur. J.*, 2019, **25**, 11157.

11 B. Kim, D. Jeong and J. Cho, *Chem. Commun.*, 2017, **53**, 9328.

12 H. Oh, W. M. Ching, J. Kim, W. Z. Lee and S. Hong, *Inorg. Chem.*, 2019, **58**, 12964.

13 B. J. Pella, J. Niklas, O. G. Poluektov and A. Mukherjee, *Inorg. Chim. Acta*, 2018, **483**, 71.

14 S. S. Nag, G. Mukherjee, P. Barman and C. V. Sastri, *Inorg. Chim. Acta*, 2019, **485**, 80.

15 (*a*) T. Tano, H. Sugimoto, N. Fujieda and S. Itoh, *Eur. J. Inorg. Chem.*, 2012, **26**, 4099; (*b*) S. Paria, T. Ohta, Y. Morimoto, T. Ogura, H. Sugimoto, N. Fujieda, K. Goto, K. Asano, T. Suzuki and S. Itoh, *J. Am. Chem. Soc.*, 2015, **137**(34), 10870.

16 (*a*) I. Monte Pérez, X. Engelmann, Y. M. Lee, M. Yoo, E. Kumaran, E. R. Farquhar, E. Bill, J. England, W. Nam, M. Swart and K. Ray, *Angew. Chem., Int. Ed.*, 2017, **56**, 14384; (*b*) G. Villar-Acevedo, P. Lugo-Mas, M. N. Blakely, J. A. Rees, A. S. Ganas, E. M. Hanada, W. Kaminsky and J. A. Kovacs, *J. Am. Chem. Soc.*, 2017, **139**, 119; (*c*) J. Deutscher, P. Gerschel, K. Warm, U. Kuhlmann, S. Mebs, M. Haumann, H. Dau, P. Hildebrandt, U. P. Apfel and K. Ray, *Chem. Commun.*, 2021, **57**, 2947; (*d*) S. P. de Visser, G. Mukherjee, H. S. Ali and C. V. Sastri, *Acc. Chem. Res.*, 2022, **55**, 65; (*e*) U. K. Bagha, R. Yadav, T. Mokkawes, J. K. Satpathy, D. Kumar, C. V. Sastri and S. P. de Visser, *Chem. – Eur. J.*, 2023, **29**, e202300478; (*f*) L. Sahoo, J. K. Satpathy, R. Yadav, S. P. de Visser and C. V. Sastri, *Eur. J. Inorg. Chem.*, 2023, e202300380; (*g*) J. K. Satpathy, R. Yadav, U. K. Bagha, D. Kumar, C. V. Sastri and S. P. de Visser, *Inorg. Chem.*, 2024, **63**, 6752.

17 G. J. P. Britovsek, J. England and A. J. P. White, *Inorg. Chem.*, 2005, **44**, 8125.

18 A. W. Addison, T. N. Rao, J. Reedijk, J. van Rijn and G. C. Verschoor, *J. Chem. Soc., Dalton Trans.*, 1984, 1349.

19 (*a*) T. Tano, M. Z. Ertem, S. Yamaguchi, A. Kunishita, H. Sugimoto, N. Fujieda, T. Ogura, C. J. Cramer and S. Itoh, *Dalton Trans.*, 2011, **40**, 10326; (*b*) A. Squarcina, M. Lovisari, P. Pirovano, A. R. McDonald and M. Bonchio, *ChemCatChem*, 2025, e00511.

20 (*a*) R. Kumar, A. Maji, B. Biswas and A. Draksharapu, *Dalton Trans.*, 2024, **53**, 5401; (*b*) A. Draksharapu, A. J. Boersma, W. R. Browne and G. Roelfes, *Dalton Trans.*, 2015, **44**, 3656; (*c*) A. Chandra, V. Kumar, U. C. Garnaik,

R. Dada, I. Qamar, V. K. Goel and S. Agarwal, *ACS Omega*, 2024, **9**, 50049; (*d*) D. P. Strommen and K. Nakamoto, *J. Chem. Educ.*, 1977, **54**, 474.

21 L. Sahoo, P. Panwar, C. V. Sastri and S. P. de Visser, *ACS Org. Inorg. Au*, 2024, **4**, 673.

22 M. J. Frisch, G. W. Trucks, H. B. Schlegel, G. E. Scuseria, M. A. Robb, J. R. Cheeseman, G. Scalmani, V. Barone, B. Mennucci, G. A. Petersson, H. Nakatsuji, M. Caricato, X. Li, H. P. Hratchian, A. F. Izmaylov, J. Bloino, G. Zheng, J. L. Sonnenberg, M. Hada, M. Ehara, K. Toyota, R. Fukuda, J. Hasegawa, M. Ishida, T. Nakajima, Y. Honda, O. Kitao, H. Nakai, T. Vreven, J. A. Montgomery Jr., J. E. Peralta, F. Ogliaro, M. Bearpark, J. J. Heyd, E. Brothers, K. N. Kudin, V. N. Staroverov, R. Kobayashi, R. Normand, K. Raghavachari, A. Rendell, J. C. Burant, S. S. Iyengar, J. Tomasi, M. Cossi, N. Rega, J. M. Millam, M. Klene, J. E. Knox, J. B. Cross, V. Bakken, C. Adamo, J. Jaramillo, R. Gomperts, R. E. Stratmann, O. Yazyev, A. J. Austin, R. Cammi, C. Pomelli, J. W. Ochterski, R. L. Martin, K. Morokuma, V. G. Zakrzewski, G. A. Voth, P. Salvador, J. J. Dannenberg, S. Dapprich, A. D. Daniels, Ö. Farkas, J. B. Foresman, J. V. Ortiz, J. Cioslowski and D. J. Fox, *Gaussian 09, Revision D.01*, Gaussian, Inc., C. T. Wallingford, 2009.

23 (*a*) A. D. Becke, *J. Chem. Phys.*, 1993, **98**, 5648; (*b*) C. Lee, W. Yang and R. G. Parr, *Phys. Rev. B:Condens. Matter Mater. Phys.*, 1988, **37**, 785; (*c*) S. Grimme, J. Antony, S. Ehrlich and H. Krieg, *J. Chem. Phys.*, 2010, **132**, 154104.

24 (*a*) P. J. Hay and W. R. Wadt, *J. Chem. Phys.*, 1985, **82**, 270; (*b*) M. M. Francl, W. J. Pietro, W. J. Hehre, J. S. Binkley, M. S. Gordon, D. J. DeFrees and J. A. Pople, *J. Chem. Phys.*, 1982, **77**, 3654.

25 J. Tomasi, B. Mennucci and R. Cammi, *Chem. Rev.*, 2005, **105**, 2999.

26 H. S. Ali and S. P. de Visser, *Chem. – Eur. J.*, 2022, **28**, e202104167.

27 *Purification of Laboratory Chemicals*, ed. D. D. Perrin, Pergamon Press, Oxford, 1997.

28 (*a*) L. Sahoo, Y. Zhang, A. Das, S. P. de Visser and C. V. Sastri, CCDC 2394154: Experimental Crystal Structure Determination, 2025, DOI: **10.5517/ccdc.csd.cc2lc9s2**; (*b*) L. Sahoo, Y. Zhang, A. Das, S. P. de Visser and C. V. Sastri, CCDC 2394155: Experimental Crystal Structure Determination, 2025, DOI: **10.5517/ccdc.csd.cc2lc9t3**; (*c*) L. Sahoo, Y. Zhang, A. Das, S. P. de Visser and C. V. Sastri, CCDC 2394156: Experimental Crystal Structure Determination, 2025, DOI: **10.5517/ccdc.csd.cc2lc9v4**.